Journal of Structural Geology, Vol. 15, No. 12, pp. 1471 to 1484, 1993
Printed in Great Britain

0191-8141/93 $06.00+0.00
© 1993 Pergamon Press Ltd

Modelling of near-field subsurface displacements for generalized faults and fault arrays

X. Q. MA and N. J. KUSZNIR

Department of Earth Sciences, University of Liverpool, P.O. Box 147, Liverpool L69 3BX, U.K.

(*Received* 13 *July* 1992; *accepted in revised form* 24 *November* 1992)

Abstract—A quantitative mathematical model using elastic dislocation theory has been developed to model the near-field subsurface displacement field associated with faults and fault arrays within an elastic layer above an elastic half-space. The three components of displacement in the spatial domain are expressed as a sum of Fourier–Bessel integrals in the wave number domain. A numerical technique using matrix decomposition has been used to obtain near-field stable solutions. Fault displacements may be dip-slip, strike-slip and oblique-slip. The model has been used to determine the three-dimensional surface and subsurface displacement fields for a rectangular fault with constant slip, and for an elliptical fault on which the slip varies from the point of maximum displacement at the centre to zero displacement at an elliptical tip-line. The three-dimensional displacement field may be determined for individual slip events on a fault, or for cumulative fault displacements. The model has also been applied to multiple fault arrays.

INTRODUCTION

THE static coseismic increment of deformation associated with earthquake faults has been studied extensively using elastic dislocation theory. Many methods based on the elastic dislocation theory are available to calculate surface displacements for a homogeneous half-space (Chinnery 1961, Maruyama 1964, Press 1965, Mansinha & Smylie 1971, Okada 1985) and for a layered half-space (Ben-Menahem & Gillon 1970, Sato 1971, Jovanovich *et al.* 1974a, Rundle 1982). The main aims of previous studies have been to interpret geodetic observations and to derive earthquake source parameters such as rupture zone size, depth of hypocentre, seismic moment and stress drop (Savage & Hastie 1966, Mikumo 1973).

The elastic dislocation theory has also been used to compute subsurface displacement for an infinite half space (Masinha & Smylie 1971, Iwasaki & Sato 1979, Okada 1992). Roth (1990) derived kernel functions for subsurface displacements above a point source within a layered elastic medium. Recently Ma & Kusznir (1992) extended Roth's theory further to compute the displacement field at any point below a fault in the upper elastic layer. This new mathematical formation permits three-dimensional displacements to be determined at the free surface, or in the subsurface either above or below the source.

In studying the deformation generated by a finite size fault using elastic dislocation theory, most workers have assumed that the fault surface is a rectangular plane with constant slip. Real faults do not however possess a rectangular geometry, neither do they have constant displacements. The new elastic dislocation model of three-dimensional subsurface displacement developed by Ma & Kusznir has been applied to a more realistic fault geometry and fault plane displacement field distribution (Ma & Kusznir 1992).

The objective of the work described in this paper is to show the three-dimensional subsurface displacement field distribution for generalized faults: dip-slip; strike-slip; and oblique-slip. Two different fault geometry and displacement distributions are considered: a rectangular fault with constant slip; and an elliptical fault with displacement distribution in which the slip varies from a point of maximum displacement at the centre to zero displacement at an elliptical tip-line, as suggested by the fault growth model proposed by Walsh & Watterson (1987). The calculated displacements for a rectangular fault and for an elliptical fault are compared.

As well as being applied to the cumulative fault displacement field, the new model has been used to determine the incremental displacement field associated with a single fault slip event, corresponding to a single seismic cycle. The mathematical model has also been used to determine subsurface displacement fields for multiple fault arrays. The subsurface displacements are calculated not only for horizontal horizons but also for vertical sections. Three-dimensional subsurface strains as well as displacements have been determined.

THEORY

A dislocation is a surface of discontinuity in displacement. If a cut is made inside an elastic body and a relative slip displacement is applied to the two surfaces of the cut, the elastic body will regain its stress equilibrium but will undergo spontaneous internal strains due to the discontinuous displacement across the surfaces of the cut. The strain pattern in the medium depends on the configuration of the cut and displacement distribution applied. Steketee (1958a,b) used the theorem of force–dislocation equivalence to study the strained elastic

system. He arrived at the statement that the displacement field due to a shear dislocation may be mathematically expressed by a surface integral of point-source elements of the double couple type over the entire fault surface. He then developed a Green's function method to calculate the stresses and displacements produced by a strike-slip fault. Maruyama (1964) derived the remaining five sets of Green's functions which allow the displacement field, due to an arbitrary displacement dislocation in a semi-infinite medium, to be determined. The practical applications of the dislocation theory to rectangular earthquake faults in an elastic half-space were addressed by Chinnery (1961), Savage & Hastie (1966) and Mansinha & Smylie (1971). Ben-Menahem & Singh (1968) extended the results of Steketee (1958a,b) and Maruyama (1964) to a layered half-space. Singh (1970) applied the Thomson–Haskell propagator matrix technique to solve the problem of the static deformation of a multi-layered elastic half-space. Each layer of the multi-layered medium is assumed to be homogeneous and isotropic, and interfaces are assumed to be in welded contact. The point source is represented as a discontinuity in the depth dependent coefficients of the displacement and stress integrands at the source level.

In the following work the modelling of displacements due to earthquake faulting using elastic dislocation theory will be restricted to the static problem only. Waves and transient dynamic features associated with the earthquake will be neglected. It is also assumed that the effects of the earth's curvature, its gravity and temperature on the displacement field are negligible. The elastic continuum will also be assumed to be isotropic so that the laws of classical linear elasticity apply.

The vector displacement $\mathbf{u}$ satisfies the Navier equation of static elasticity for an uniform, infinite space:

$$[\nabla^2 + (1 + \lambda/\mu)\, grad\, div]\, \mathbf{u} = 0, \tag{1}$$

where λ and μ are Lamé's constants. The three independent vector solutions of (1) are listed in equation (2) of Singh (1970). The general solution of equation (1) is expressed in the spatial domain as a sum of integrals in the wave number domain:

$$\mathbf{u} = \sum_m \int_0^\infty \mathbf{u}_m(k) k \, dk, \tag{2}$$

where $\mathbf{u}_m$ is a linear combination of the three independent vector solutions (also see equation 6 in Singh 1970).

To incorporate layering effects, one has to apply: (i) the conditions of zero normal traction for the free surface; (ii) those of zero displacement, stress and potential at infinite depth; and (iii) displacement and stress continuity across layer boundaries. A source is incorporated by creating a layer boundary at the source depth and prescribing appropriate discontinuity conditions across the boundary for the source. By using the Thomson–Haskell matrix propagator technique, the displacement field expressions can be transformed to Fourier–Bessel integrals. The case for a vertical dip-slip point source is given below. The three-components of displacement are:

$$\begin{aligned} u_r &= -\int_0^\infty [(1/i) y_{11}(z_k)(\partial/\partial kr) J_1(kr) \\ &\qquad + z_{11}(z_k)(1/kr) J_1(kr)] k \, dk \sin\varphi \\ u_\varphi &= -\int_0^\infty [(1/i) y_{11}(z_k)(1/kr) J_1(kr) \\ &\qquad + z_{11}(z_k)(\partial/\partial kr) J_1(kr)] k \, dk \cos\varphi \\ u_z &= -\int_0^\infty [(1/i) x_{11}(z_k) J_1(kr)] k \, dk \sin\varphi, \end{aligned} \tag{3}$$

where x_{11}, y_{11} and z_{11} are kernel functions dependent on source dimension, depth and dislocation; J_1 is a Bessel function; z_k is depth of an observation level in the subsurface. The kernel functions of surface displacements are given in equation (41) of Singh (1970) and those of subsurface displacements have been derived by Ma & Kusznir (1992).

The evaluation of kernel functions has been carried out by decomposing matrices contained in the kernels into analytical forms, i.e. a sum of exponential-polynomials using the technique proposed by Ben-Menahen & Gillon (1970). The original displacement integrals in (3) can then be transformed to the well-known Lipshitz–Hankel integrals whose quadrature is analytical (Erdelyi 1954):

$$u(r) = \sum_l \sum_n a_{ln} \int_0^\infty k^n \, e^{(-kD_l)} J_m(kr) \, dk \tag{4}$$

(where a_{ln} are constant coefficients, and D_l are exponential arguments which are a function of layer thickness, source depth and depth of an observation point). The calculation of displacements using the method described above is fast, stable and has acceptable accuracy.

The three-dimensional displacement field for a fault of any geometry and fault surface displacement discontinuity may be determined by convolving the point source displacement field response with the fault surface displacement distribution.

In this paper, we deal with a model consisting of one elastic layer overlying an elastic half-space. Lamé's constants for the top elastic layer are: $\mu_1 = 7.0 \times 10^{10}$ N m^{-2}, $\lambda_1 = 8.22 \times 10^{10}$ N m^{-2}, and those for the infinite half space are: $\mu_2 = 1.55 \times 10^{11}$ N m^{-2}, $\lambda_2 = 1.82 \times 10^{11}$ N m^{-2}. The results can be extended to a multi-layer model by introducing extra layer matrices. We use the newly derived mathematical formulation to determine displacements for generalized faults and fault arrays.

The following convention is adopted for the single fault displacement calculation: the fault dips down towards the positive Y direction; the strike of the fault is taken along the X axis; the length of the fault is defined as the dimension in the strike direction while the width is defined as the dimension normal to strike.

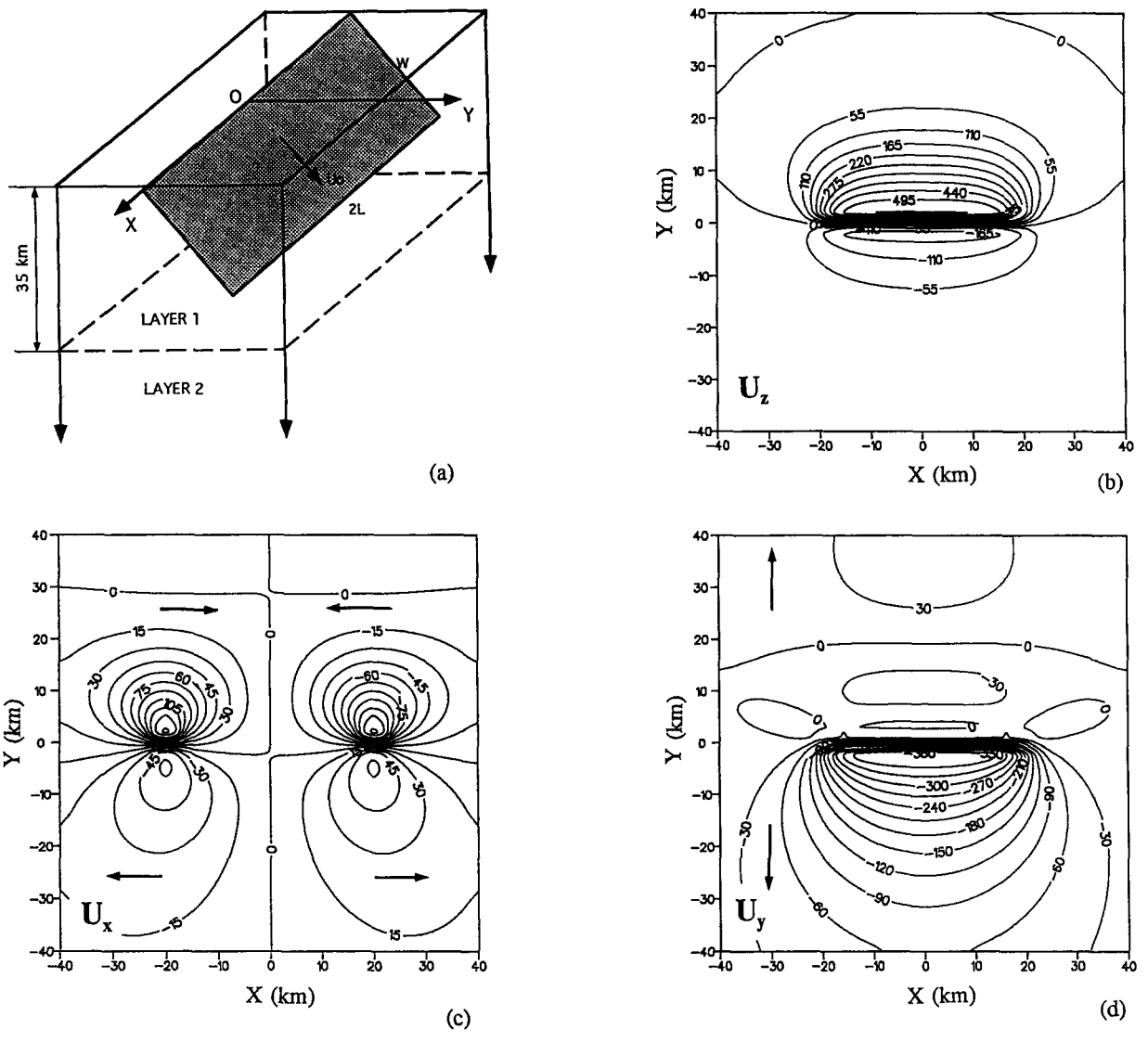

Fig. 1. (a) Co-ordinate system and geometry of a rectangular dip-slip fault of length $2L = 40$ km and width $W = 20$ km. The fault dips at 60° towards the positive Y direction and intersects the free surface ($D = 0$). The slip is constant ($U_0 = 1$ km). The thickness of the top elastic layer is 35 km. The elastic properties of the medium are described in the text. (b) Vertical surface displacement (U_z) contour map. (c) Horizontal surface displacement (U_x). (d) Horizontal displacement (U_y). Note that the displacement values are in metres while the labelled numbers on axes are in km. This notation is applied to all figures in this paper.

RECTANGULAR DIP-SLIP FAULT WITH CONSTANT SLIP

The surface displacement field for a rectangular planar fault with constant slip is shown in Fig. 1. The 60° dip-slip fault cuts through the upper part of the top layer and intercepts the free surface. The arrows on the diagrams indicate the directions of material movement. The material on the downthrow side in Fig. 1(c) moves inwards while on the upthrow side they move outwards. One of the conspicuous features in Fig. 1(b) is the asymmetry of the displacement contour pattern, i.e. the uplift marked by negative vertical displacement values are relatively small compared to the subsidence. The degree of this asymmetry varies with fault dip.

Subsurface vertical displacements are shown in Fig. 2 for a blind rectangular fault. The fault dips at 60°, and its top is at depth $D = 8$ km from the free surface. The locations of three vertical sections (AB, CD, EF) are shown in Fig. 2(a). Sections AB and CD are normal to the strike of the fault, while section EF is parallel to the strike. Section AB cuts the fault through its centre. Figure 2(b) is the vertical displacement contour map along section AB, and shows the deformation on both sides of the fault. Positive contour values correspond to subsidence while negative values correspond to uplift. Note that the straight line formed by the zero displacement contour within the fault zone is at an angle of 60° with the horizontal, and exactly corresponds to the prescribed dip of the fault. Displacements on each side of the fault are maximum adjacent to the fault.

Figure 2(c) shows the vertical displacement contour map on the vertical section CD which is 2 km away from the edge of the fault. In comparison with (b), it can be seen that the displacement values for this section are significantly reduced. Furthermore, the point of maximum displacement on the downthrow side has moved upwards, while the point of maximum displacement on

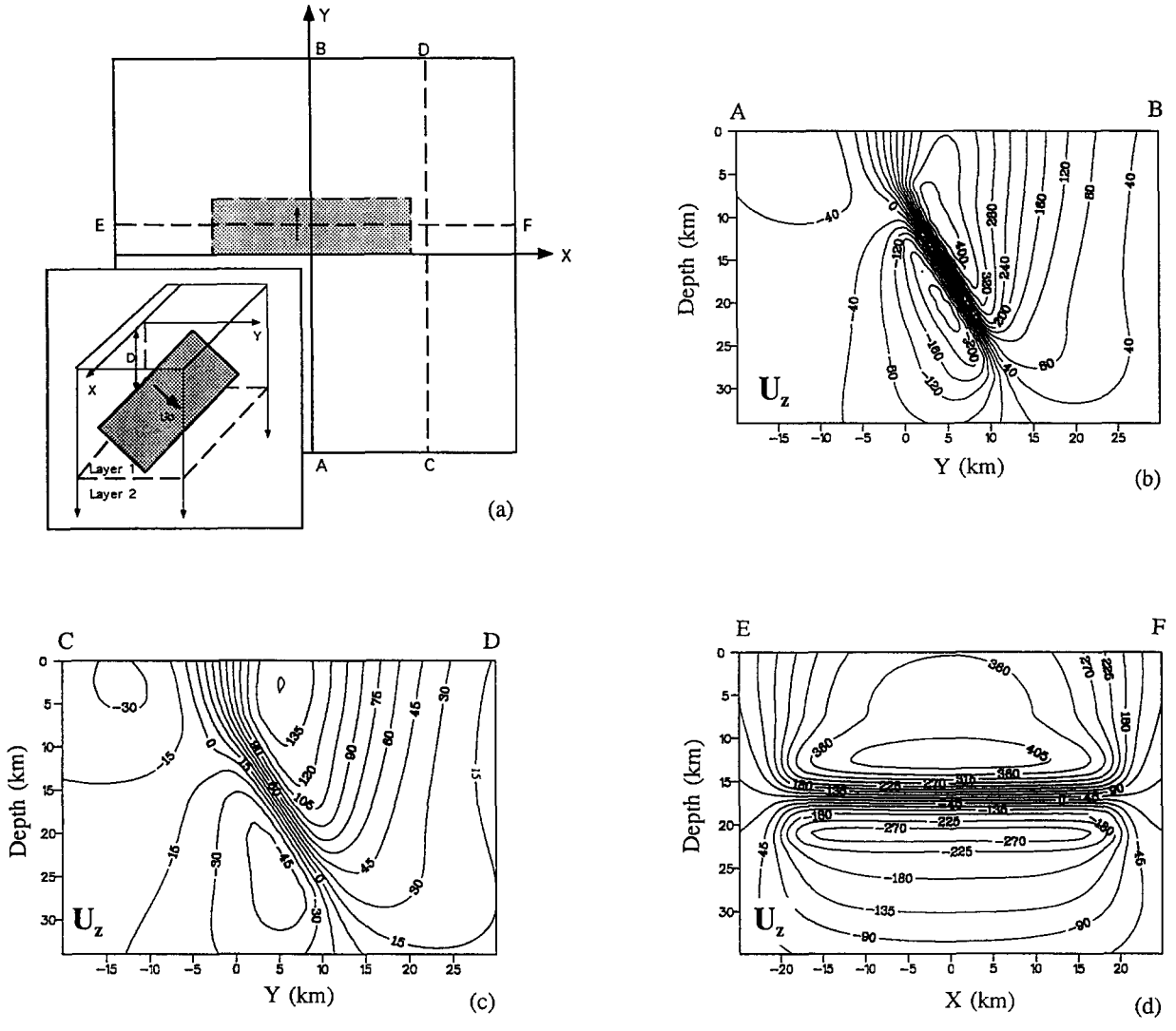

Fig. 2. (a) Plan view of a buried rectangular fault and three vertical sections. The fault is at depth $D = 8$ km. Sections AB and EF cut through the fault centre. (b) Vertical displacement contour map along section AB ($x = 0$ km). (c) Vertical displacement along section CD ($x = 22$ km). (d) Vertical displacement along section EF ($y = 5$ km).

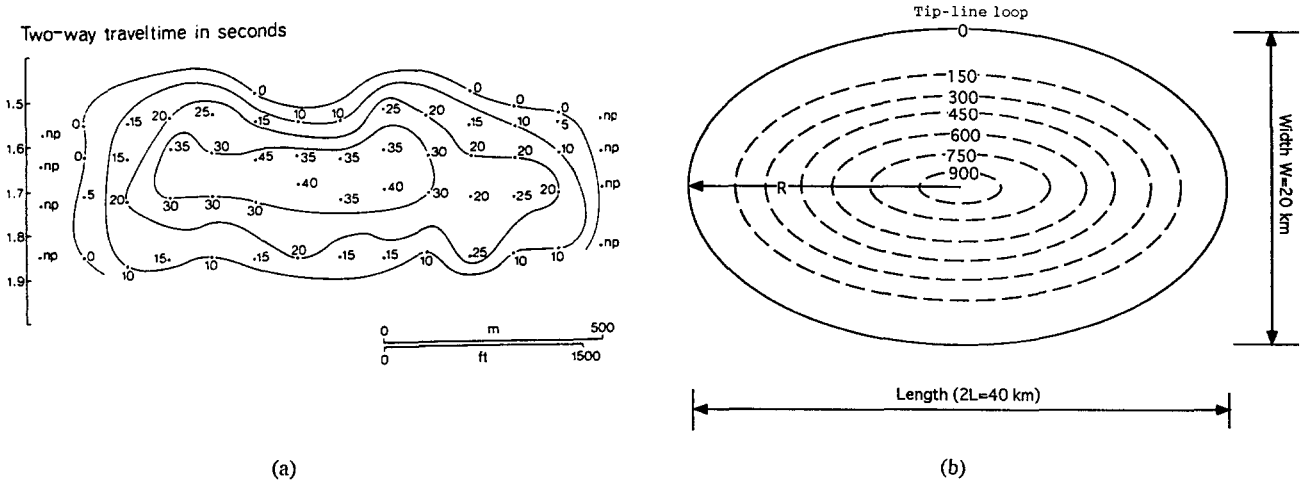

Fig. 3. (a) Contour displacement diagram for a fault from the U.K. North Sea basin (from Barnett *et al.* 1987). Displacement values include displacements on several synthetic splays. Vertical displacement measured as two-way travel time (ms) with resolution of 5 ms; *np* denotes fault not present. (b) Cumulative displacement geometry for the elliptical fault growth model (Wash & Watterson 1987) with long axis 40 km and short axis 20 km. Note that the slip (in metres) varies from a point of maximum displacement (1 km) at the centre to zero displacement at elliptical tip-line.

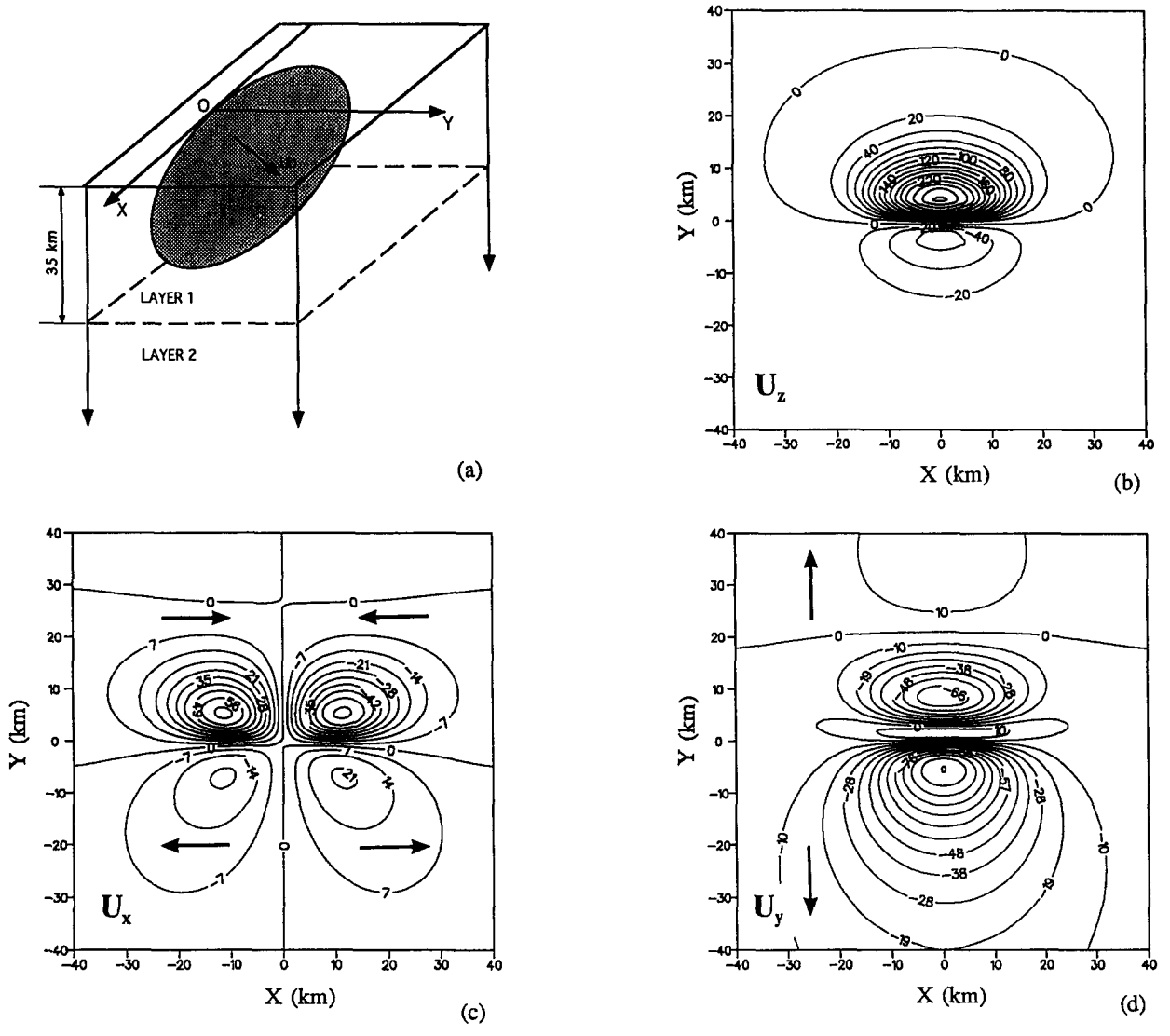

Fig. 4. (a) Geometry of an elliptical dip-slip fault with cumulative displacement distribution. The maximum displacement at the centre is 1 km. The fault dips at 60° towards the positive Y direction and intersects the free surface ($D = 0$). The observation horizon is the free surface. (b) Vertical surface displacement (U_z) contour map. (c) Horizontal surface dispacement (U_x). (d) Horizontal surface displacement (U_y).

the upthrow side of the fault has moved downwards. Although the section does not intersect the fault surface, a fault zone indicated by closed displacement contours is still apparent. Figure 2(d) is the displacement contour map on the vertical section EF parallel to the fault, and shows two concentric elliptical contour lines within the footwall and hanging wall. The zero displacement contour line corresponds to the level of the fault centre, which is at a depth of 16.6 km.

ELLIPTICAL FAULT WITH CUMULATIVE DISPLACEMENT

Dip-slip fault

Field observations and seismic reflection data show that fault surfaces, whether for blind faults or ones intersecting the free surface, are never rectangular, nor are the displacements constant. Fault geometry and displacement data extracted from coal mine records and high-resolution seismic reflection data show a systematic displacement variation for blind faults with fault dying out upwards, downwards and laterally. Figure 3(a) is a strike projection showing fault displacement for a blind fault from the U.K. North Sea basin, constructed by projecting displacement values at points on a fault surface onto a surface parallel to the fault strike (Barnett *et al.* 1987). An idealized blind fault has an elliptical fault surface defined by the zero displacement contour, and displacement which varies from a point of maximum displacement at the centre to zero displacement at the tip-line. Contours of equal displacement form ellipses centred on the point of maximum displacement. The displacement gradient normally varies with direction on the fault surface, the ellipse usually being elongated laterally. Figure 3(b) shows the displacement contours for an idealized blind fault corresponding to those of the Walsh & Watterson fault growth model (Watterson 1986, Walsh & Watterson 1987). The fundamental concept of the Walsh & Watterson fault growth model is that the slip increases linearly with fault radius as the

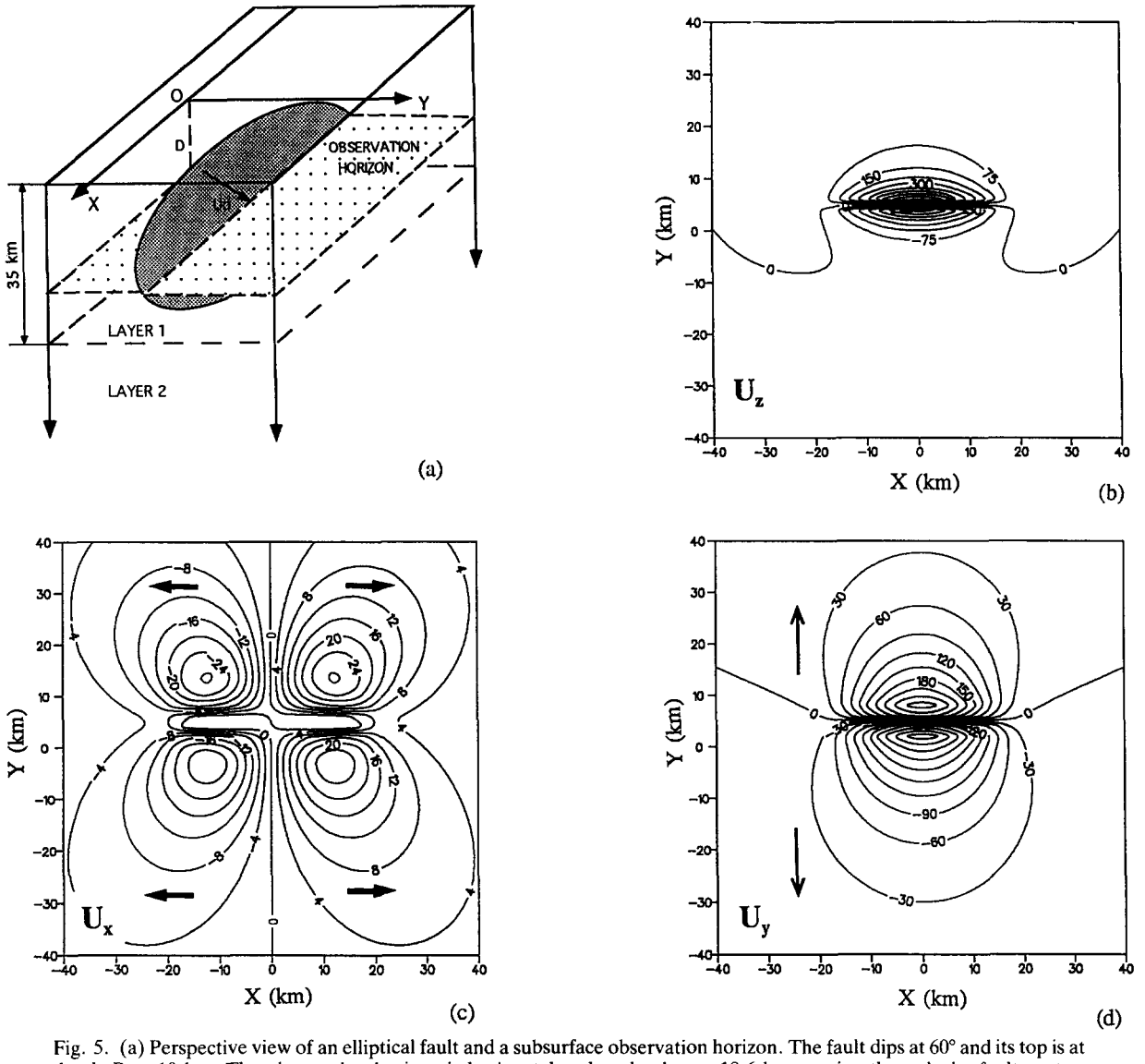

Fig. 5. (a) Perspective view of an elliptical fault and a subsurface observation horizon. The fault dips at 60° and its top is at depth D = 10 km. The observation horizon is horizontal and at depth z = 18.6 km, cutting through the fault centre. (b) Vertical displacement (U_z) contour map. (c) Horizontal displacement (U_x). (d) Horizontal displacement (U_y).

fault grows so that the maximum total displacement increases with the square of the fault length. For a blind fault grown by multiple slip events in which the maximum slip in successive slip events increases by a constant amount, the cumulative displacement can be calculated using the formula derived by Walsh & Watterson (1987). The displacement distribution shown in Fig. 3(b) has been used in the following elastic dislocation model displacement calculation.

The computation procedures are similar to those for a rectangular fault. The displacement geometry differs in that the displacement across the fault surface now varies from point to point, rather than having a constant value for a rectangular fault. Unit slip is assumed for all the point sources followed by linear scaling to incorporate displacement variation as determined by the fault growth model.

Figure 4 shows the vertical and horizontal surface displacement contour maps calculated for the elliptical fault growth model described above and shown in Fig. 3(b). The fault dips at 60° and intersects the free surface. It can be seen that the displacement values and deformed area, in any one of the contour maps, are smaller than those of the rectangular constant slip fault (Fig. 1). The concentric ellipse-like contours formed by equal horizontal displacement (U_x) and shown in Fig. 4(c) are closer to each other than those for the rectangular fault. For the vertical displacement (U_z), the closed contours on both sides of the fault are less flattened for the elliptical fault growth model (Fig. 4b) than for the constant slip model (Fig. 1b). The asymmetry of vertical displacements on both sides of the fault is still apparent.

Fault dip controls the displacement distribution and as a consequence the symmetry–asymmetry of displacement patterns on the down-throw and up-throw sides. It is well known that a vertical dip-slip fault displays an antisymmetry in vertical displacements between up-throw and down-throw sides. Any fault whose dip is less than 90° will show an asymmetry in vertical displacements, and the asymmetry increases with decreasing fault dip. This assymmetry is such that fault uplift is reduced relative to subsidence for a normal fault. At the

same time, a decrease in fault dip is accompanied by a decrease in the vertical component of displacements. The ratios of the maximum amount of uplift to the maximum amount of subsidence on the free surface are about 1, 9, 24 and 100%, for the dip-slip elliptical fault growth model with dips of 30°, 45°, 60° and 90°, respectively, and are about 7, 20, 40 and 100% for a rectangular fault of constant slip with the same dimension and dips. The ratios of maximum uplift to maximum subsidence and their dependence on fault dip are therefore different for the elliptical fault growth and the rectangular constant slip fault models.

Subsurface fault displacement patterns differ profoundly from those of the surface. The displacement contour pattern is shown in Fig. 5 on a subsurface horizontal plane which intersects the centre of an elliptical blind fault. Figure 5(a) is a perspective view of a blind fault and a subsurface horizon. The blind fault again dips at 60° and has a depth of 10 km below the free surface to the top of the fault. Figures 5(b)–(d) show the three components of displacements at a depth of 18.6 km. The fault displacement geometry is otherwise the same as in Fig. 3(b). Positive values in Fig. 5(b) correspond to subsidence, while the negative values correspond to uplift. Note that although the horizon crosses the centre of the fault, the vertical displacement contour patterns are not symmetric on the down-throw and up-throw sides, i.e. there is a greater amount of subsidence than uplift. This is because the depth of the fault (10 km) is not sufficiently great, compared to the dimension of the fault (width 20 km), to eliminate free surface effects. It has also been found that the ratio of uplift to subsidence increases with an increase of fault depth. Symmetry is only expected when the fault depth is much greater than the fault dimension. A striking feature of the horizontal displacement (U_x) contour map of Fig. 5(c) for the elliptical fault growth model is that, in contrast to the similar map in Fig. 1(c) for the rectangular fault with constant slip, the fault growth model shows outward movement in a direction parallel to strike on both sides of the fault. The displacement contour patterns of U_y for the elliptical fault growth model are almost symmetric with respect to the fault plane.

Vertical sections of the vertical displacement for the

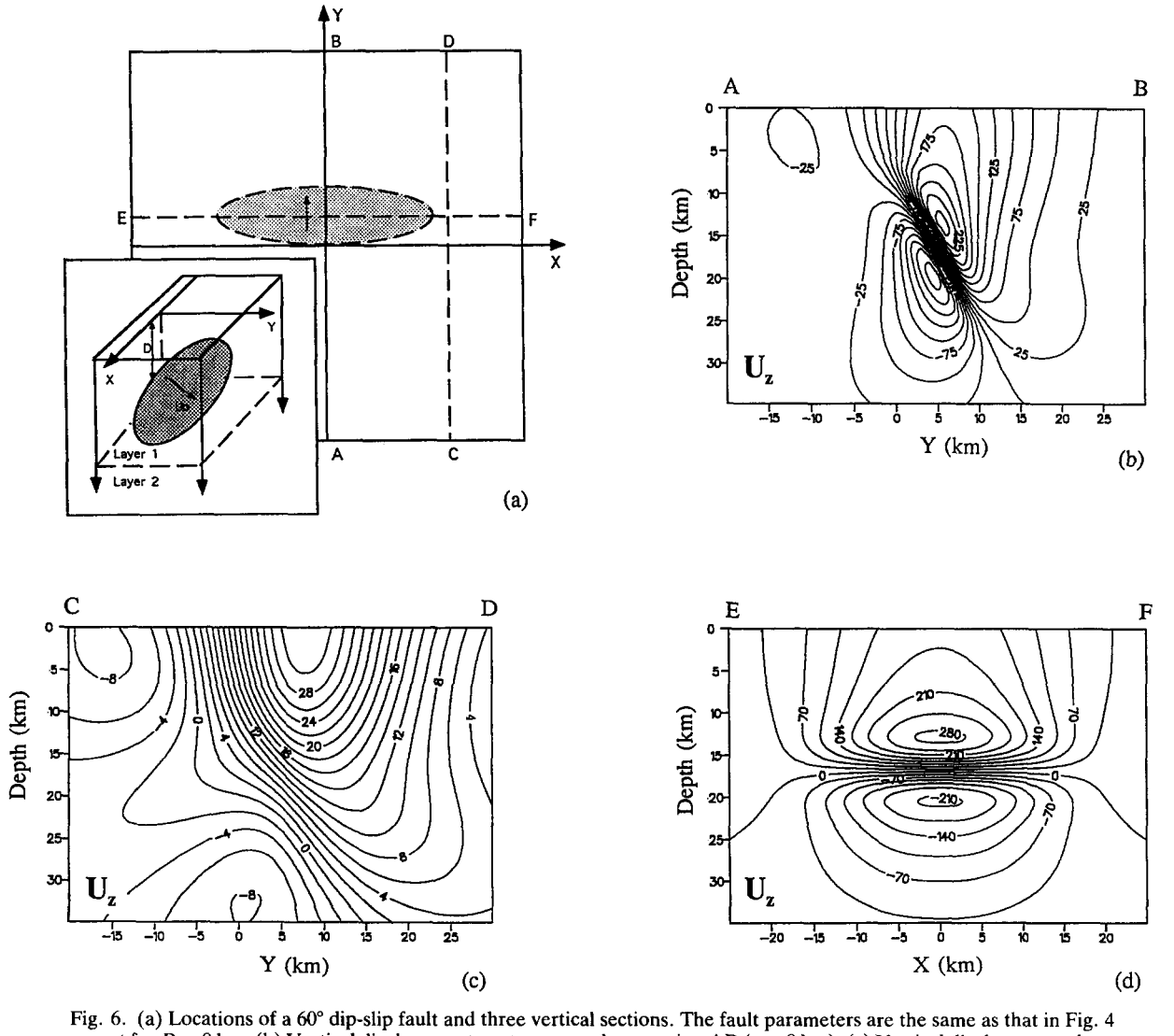

Fig. 6. (a) Locations of a 60° dip-slip fault and three vertical sections. The fault parameters are the same as that in Fig. 4 except for D = 8 km. (b) Vertical displacement contour map along section AB (x = 0 km). (c) Vertical displacement along section CD (x = 22 km). (d) Vertical displacement along section EF (y = 5 km).

buried elliptical fault growth model are shown in Fig. 6. The locations of the vertical profiles are shown in Fig. 6(a). The general characteristics of contour patterns for profiles AB and EF are similar for the elliptical fault growth and rectangular fault models except for the reduced displacement values of the elliptical fault growth model. The two points of maximum displacements on both sides of the fault in Fig. 6(b) are closer for the elliptical fault growth model than for the rectangular fault. A conspicuous fault zone is no longer evident for profile CD which passes by the side of the elliptical fault. This is because the displacement distribution for the elliptical fault growth model has lower strains near the edge of the fault.

Strike-slip fault

The displacement due to a dipping strike-slip fault is a linear combination of displacements from a vertical strike-slip and a vertical dip-slip fault. Figure 7 shows the three components of surface displacement for a 60° strike-slip fault. The fault geometry and displacement distribution are taken the same as in Fig. 4 except for a different slip direction. The 'bone'-shaped contour patterns for the two horizontal displacements (U_x, U_y) are similar to those for a vertical strike-slip fault described by Chinnery (1961). Displacement contours show asymmetry, in contrast to a vertical strike-slip fault which shows an anti-symmetric pattern. The displacement gradient in the hanging wall block for each displacement component is always higher than that in the footwall block. Figure 7(c) shows that the primary motion of this strike-slip fault is horizontal and along strike.

Vertical sections of the horizontal displacement (U_x) for a 60° strike-slip fault are shown in Fig. 8. Sections AB and CD are normal to strike while section EF is parallel to strike. Positive displacement values indicate the direction of material movement is out of the paper, while negative values indicate the direction is into the paper. Profile AB shows two closure regions of displacement contours separated by a zero displacement contour. The contours on both sides of the fault are almost symmetric which may indicate that the free surface effect is less for the horizontal displacement of a strike-

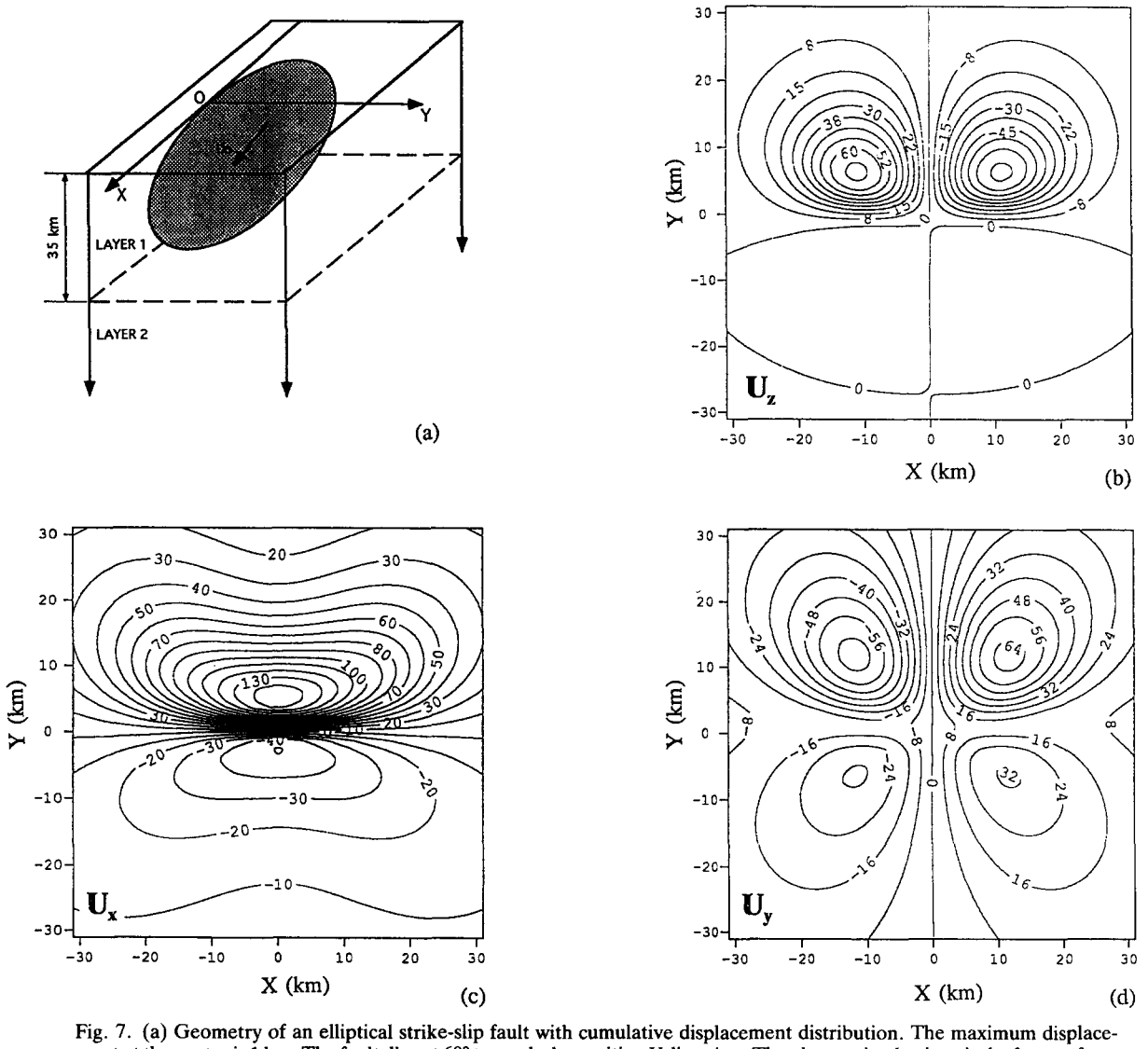

Fig. 7. (a) Geometry of an elliptical strike-slip fault with cumulative displacement distribution. The maximum displacement at the centre is 1 km. The fault dips at 60° towards the positive Y direction. The observation horizon is the free surface. (b) Vertical surface displacement (U_z) contour map. (c) Horizontal surface displacement (U_x). (d) Horizontal surface displacement (U_y).

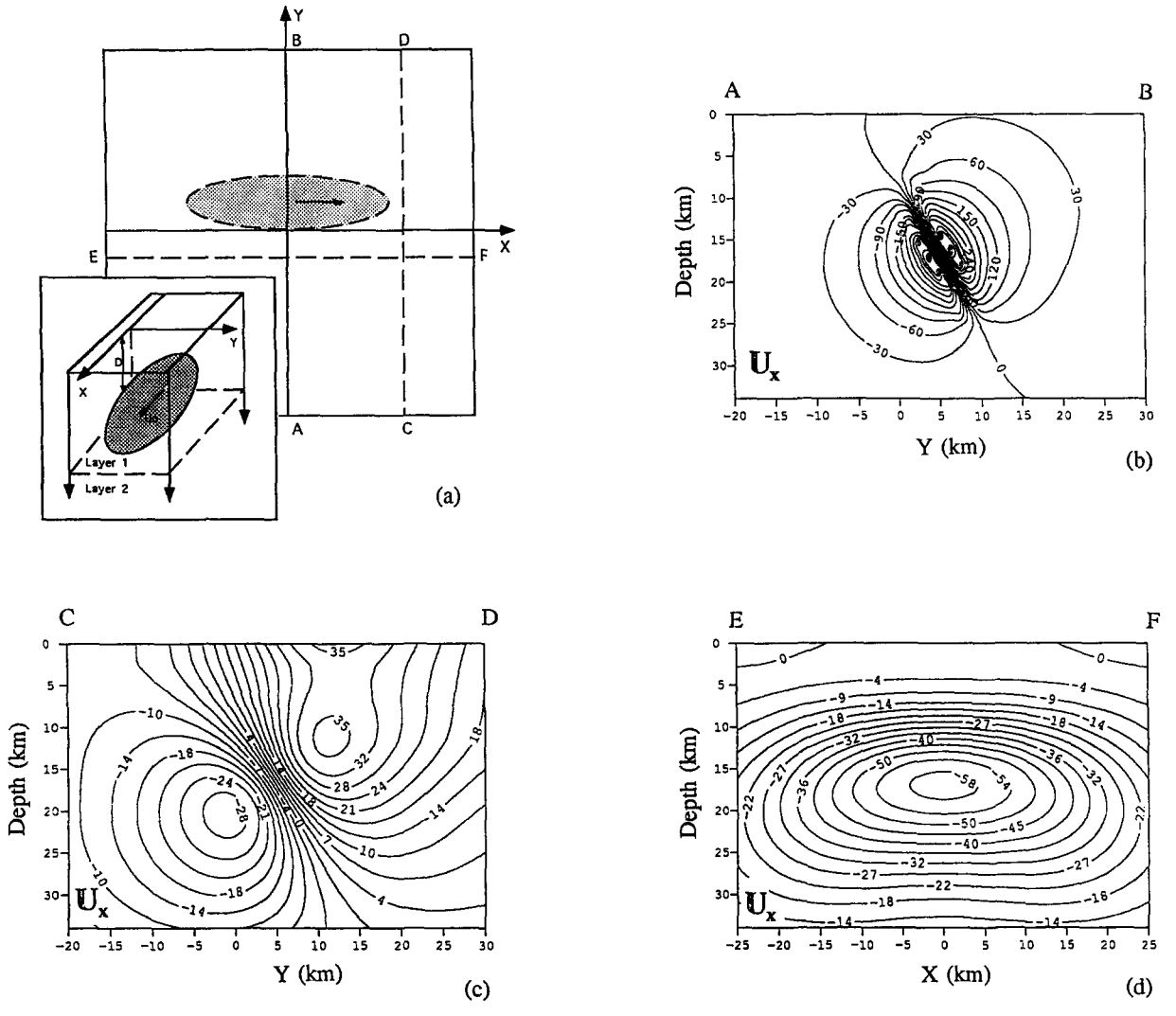

Fig. 8. (a) Locations of a strike-slip fault and three vertical sections. The fault parameters are the same as that in Fig. 7(a) except for $D = 8$ km. (b) Horizontal displacement contour map along section AB ($x = 0$ km). (c) Horizontal displacement along section CD ($x = 22$ km). (d) Horizontal displacement along section EF ($y = -5$ km).

slip fault than for the vertical displacement of a dip-slip fault (refer to Fig. 6b). Profile CD, 2 km away from the edge of the fault, shows reduced displacement values. Profile EF shows concentric elliptical contour lines.

Oblique-slip fault

So far, only dip-slip and strike-slip faults have been examined. The model can also be applied to a fault with oblique slip. The rake β is defined as an angle formed by the slip direction and the strike of the fault, and can be chosen as any values from 0° to 360°. If $\beta = 0°$, the fault is strike-slip; if $\beta = 90°$, the fault is dip-slip; if $\beta = 270°$, the fault is a thrust fault. Mathematically, the displacements due to an oblique-slip fault is a linear combination of displacements from a vertical strike-slip, a vertical dip-slip and a 45° dip-slip faults. Figure 9 shows the surface displacement contours for an oblique-slip fault intersecting the free surface. The fault has an elliptical shape and displacement gradient. The fault parameters are the same as in Fig. 4 except for $\beta = 45°$. As would be expected there is a substantial difference in contour patterns compared to the pure dip-slip and strike-slip examples.

SINGLE SLIP FAULT EVENT

Slip refers to the fault displacement increment occurring during a single seismic event or cycle. Walsh & Watterson (1987) suggest that the maximum slip increases linearly with fault radius, whereas maximum total displacement increases approximately with the square of the fault radius. The pattern of normalized displacement vs normalized distance from the centre of the fault is therefore different for the total displacement and individual event slip. Figure 10(a) shows the fault surface displacement distribution for a single slip fault event where the slip varies from a point of maximum slip (1 m) at the centre to zero slip at the tip-line. The slip contour pattern differs from that of the total displacement distribution shown in Fig. 3(b). Specifically, the slip gradient (change in displacement/radial distance) is

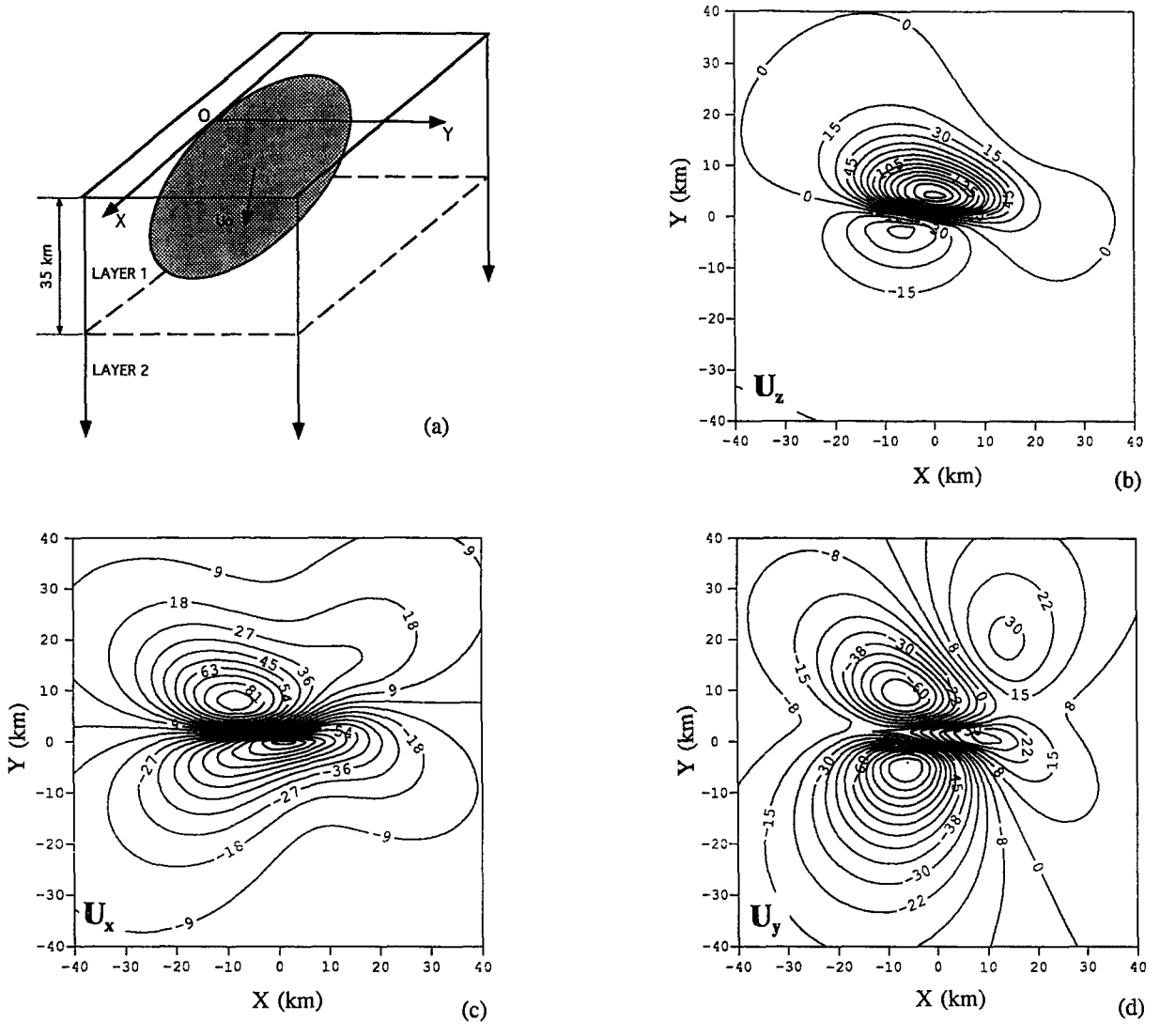

Fig. 9. (a) An oblique-slip fault dipping at 60°. The displacement geometry is the same as defined in Fig. 4 except for the rake β = 45°. The observation horizon is on the free surface. (b) Vertical displacement (U_z) contour map. (c) Horizontal displacement (U_x). (d) Horizontal displacement (U_y).

higher within a narrow zone adjacent to the tip-line loop of the slip surface. For simplicity and comparison, we choose a fault with the same dimension as in Fig. 4. Let us suppose we have obtained by some means the surface slip distribution of an active fault for the nth slip event as shown in Fig. 10(a). The three-dimensional displacement field increment may be determined using the same numerical technique as described in the last section. The calculated three-dimensional surface displacements are shown in Fig. 10. The closed contours for vertical displacements on both sides of the fault are more flattened for the single slip event than for the cumulative displacement fault. The horizontal displacement contour patterns however resemble those of total displacement profile of the elliptical fault (Fig. 4).

FAULT ARRAYS

It is rare to see a single isolated fault. Geological observation shows that the displacement fields of adjacent faults overlap, and that structure contours are resultants of displacements on multiple faults. To obtain the overall pattern of displacement contour maps for two or more faults, we must first determine the displacement field of isolated single faults separately. The composite displacement field may then be obtained by superposition of the displacement fields of individual faults. Figure 11 shows the total vertical displacements due to multiple dip-slip faults intersecting the free surface. The fault geometry and displacement distribution are the same as those of Fig. 4, except that the maximum displacement at the fault centre is 2 km rather than 1 km.

Figure 11(a) shows the total displacement due to two parallel faults both dipping in the same direction towards 225°. The negative displacement values indicate uplift, while the positive values in the lower part of the diagram indicate subsidence. Within the relay zone, where the faults overlap, a ramp-type geometry exists. Figure 11(b) shows the overall displacement due to two parallel faults which dip towards each other forming a full graben with peripheral highs. Figure 11(c) shows two faults which have opposing dips forming two

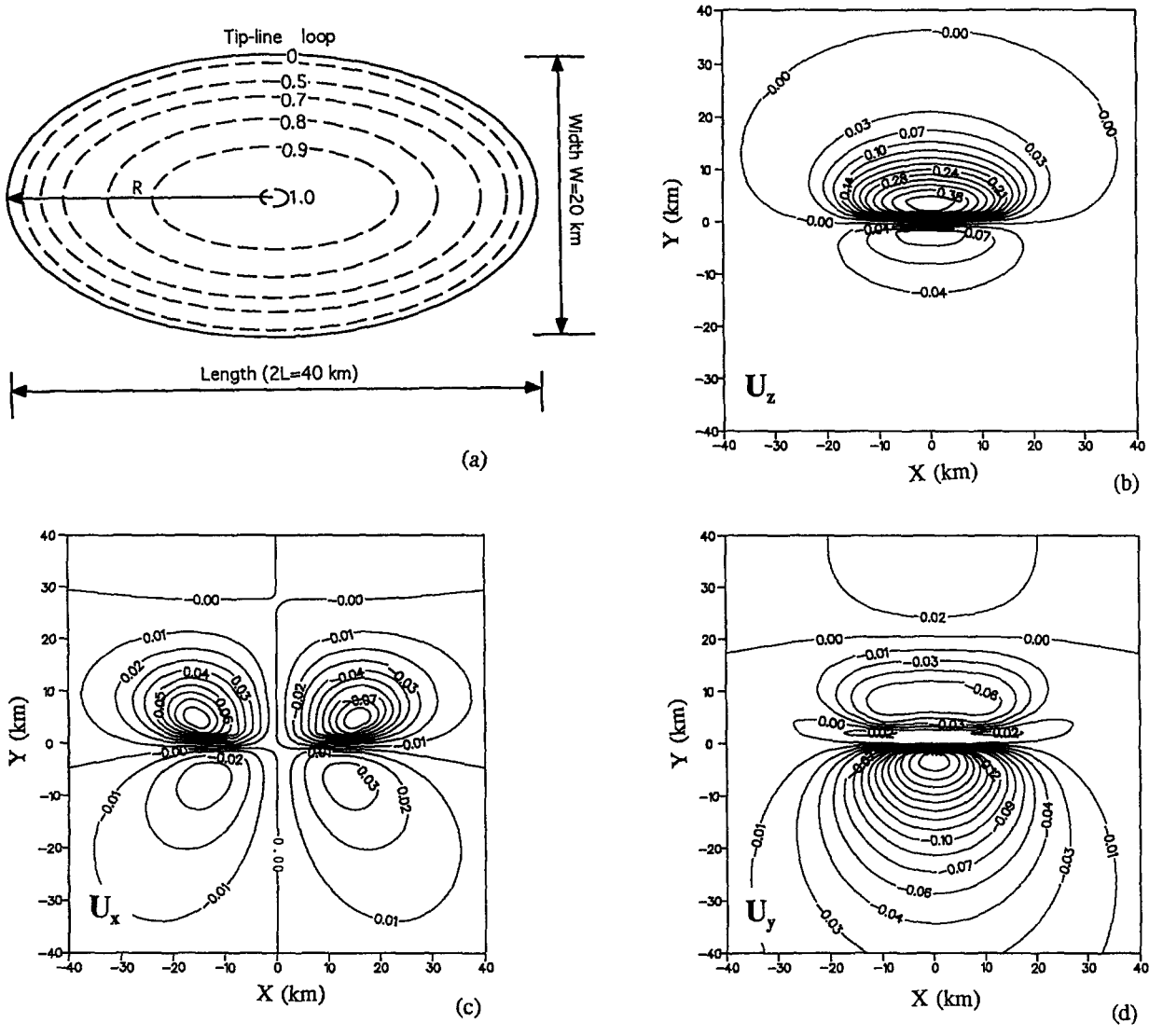

Fig. 10. (a) Displacement geometry on a single slip event fault dipping at 60° towards the positive Y direction. The fault length $2L = 40$ km, and width $W = 20$ km. The maximum slip at the centre is 1 m. (b) Vertical surface displacement (U_z) contour map. (c) Horizontal surface displacement (U_x). (d) Horizontal surface displacement (U_y).

outward facing half grabens separated by a central horst. Figure 11(d) shows the displacement distribution due to three separate faults where the outer faults both dip towards 45°, while the central fault dips towards 225°. The displacement pattern of Fig. 11(d) shows, along a profile from 45° to 225°, a half graben, a horst and a full graben.

Figure 12 shows contours of vertical displacements for two parallel elliptical faults of various relative polarities. The vertical section is along the Y axis perpendicular to the strike of the fault. Figure 12(b) shows vertical displacements for two parallel faults dipping in a same direction and a highly deformed region is shown between the faults. Figures 12(c) & (d) show vertical displacements for faults of opposite polarity dipping outwards and inwards, corresponding to a horst bounded by two half grabens and a full graben, respectively.

The theory described in this paper may be applied to fault systems with faults of any number, relative orientation, slip and dimension.

DISCUSSION

Using the elastic dislocation theory, we have modelled cumulative coseismic deformation associated with earthquake faults created by a large number of seismic cycles. The model does not however consider the gravitational effects relating to positive or negative surface topography, lower-crustal thinning, lithosphere temperature field perturbation, erosion and deposition of sediment. These loads, whether positive or negative, will result in regional scale isostatic uplift and/or subsidence. The isostatic loading effects for a normal or a thrust fault cutting the free surface are greater than for a blind fault, because they generate greater surface subsidence and culmination than blind faults. The elastic dislocation model described in this paper does not take into account interseismic deformation due to the relaxation of stresses in the viscoelastic layers of the lower crust and mantle, nor its modification by isostasy, which play a large role in controlling the final crustal structure equilibrium.

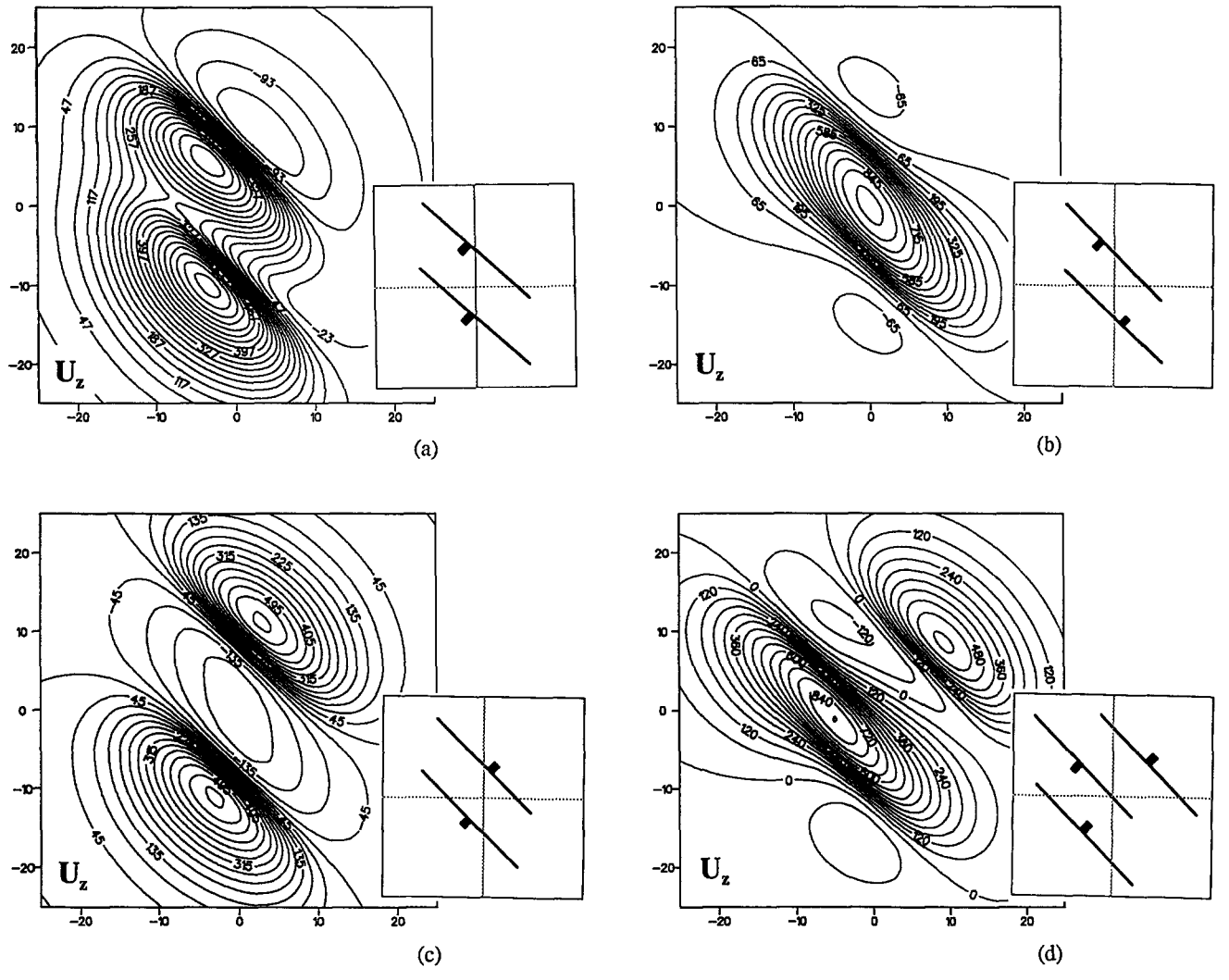

Fig. 11. Total vertical displacement contour maps due to fault arrays. Faults all dip at 60° and intersect the free surface. The individual fault displacement geometry is the same as in Fig. 4 except for the maximum displacement 2 km. The observation horizon is on the free surface. (a) Vertical displacement due to two faults both dipping towards 225°. (b) Vertical displacement due to two faults dipping towards each other. (c) Vertical displacement due to two faults dipping away from each other. (d) Vertical displacement due to three faults with the side ones dipping towards 045° and the middle one dipping towards 225°.

So far, only planar fault have been considered. In practice, fault dips may vary with depth and with formation lithology. The variation of fault curvatures will affect the displacement geometry on the fault and control the displacement fields within a medium surrounding a fault. It is anticipated that future fault models of subsurface displacement will be able to take into account viscoelastic and isostatic effects as well as variable fault curvature.

While the model formulation permits layer elasticity parameters to be varied, this paper give results for an earth model with one set of elastic parameters only. Elastic properties, and in particular rigidity, exert a strong control on the displacement field. Several earlier workers have studied the effect of elastic moduli layering on fault-induced displacements (Rybicki 1971, Sato 1971, Chinnery & Jovanovich 1972, Sato & Matsu'ura 1973, Jovanovich *et al.* 1974b). Recently, Ma & Kusznir (in review) have investigated earth layering and gravitational effects on subsurface displacement using an elastic-gravitational dislocation fault model. They concluded that for a fault source within the upper layer, variations in the rigidity of lower layers controls the amplitude and wavelength of displacements within the upper layer and in particular the relative distribution uplift and subsidence within the footwall and hanging wall. Displacement variations within the upper layer, due to lower layer rigidity changes, are shown to increase with depth and are profound at the base of the upper layer.

CONCLUSIONS

(1) Using elastic dislocation theory with novel kernel functions for expressing displacements in the subsurface, it is possible to evaluate three-dimensional displacements at any point within a rock volume containing a fault.

(2) Surface and subsurface three-dimensional displacements have been calculated for an elliptical fault with cumulative displacements, and also for a rectangu-

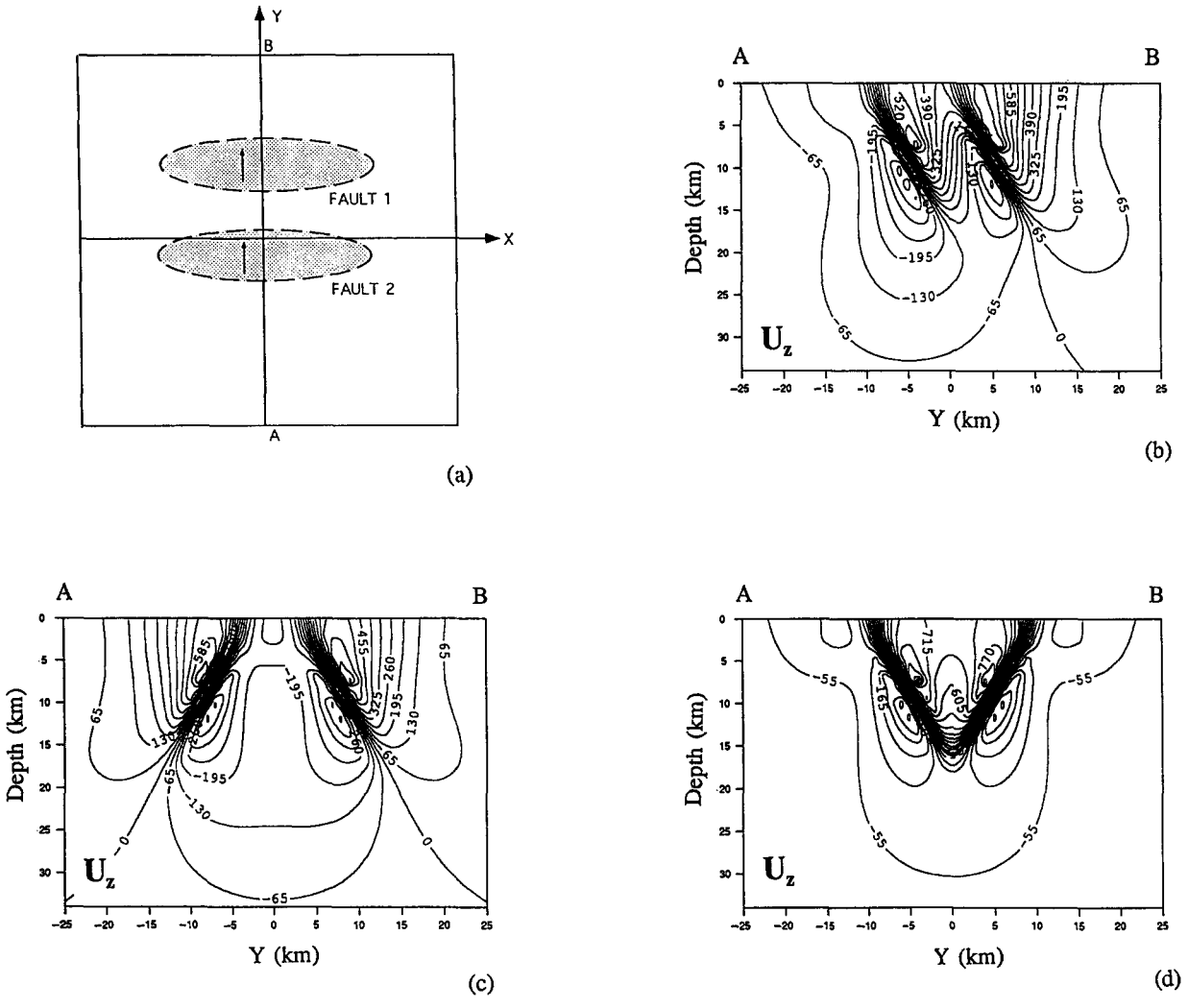

Fig. 12. (a) Plan view of two identical faults dipping towards the positive Y direction. The faults intersect the free surface. The individual fault displacement geometry is the same as in Fig. 4 except for the maximum displacement 2 km. The vertical section is along the Y axis. (b) Vertical displacement for two faults dipping in a same direction. (c) Vertical displacement for two faults dipping away from each other. (d) Vertical displacement for two faults dipping towards each other.

lar fault with constant slip. The effects of fault displacement distribution and observation horizon level on displacements have been explored.

(3) Surface and subsurface three-dimensional displacement may be determined not only for dip-slip faults but also for strike-slip and oblique-slip faults.

(4) If the slip distribution for a single slip event is known, the surface and subsurface displacements associated with that slip event may also be determined. As a consequence, the deformation associated with earthquake faulting may be used to derive earthquake parameters.

(5) The composite displacement field for a multiple fault array may be determined by superposing the displacement field of individual isolated faults. This may be applied for faults of any number, relative orientation, slip and dimension.

(6) Observed fault plane displacement distributions obtained from three-dimensional seismic reflection and mine plan data may be used to predict the three-dimensional subsurface continuum displacement field using elastic dislocation fault models.

Acknowledgements—This work is supported by the Natural Environment Research Council grant D1/G1/189/03. We appreciate helpful reviews of this manuscript by J. C. Savage and Frank Roth. We thank Juan Watterson and John Walsh for their valuable inspiration, discussion and encouragement.

REFERENCES

Barnett, J., Mortimer, J., Rippon, J. H., Walsh, J. J. & Watterson, J. 1987. Displacement geometry in the volume containing a single normal fault. *Bull. Am. Ass. Petrol. Geol.* **71**, 925–937.

Ben-Menahen, A. & Gillon, A. 1970. Crustal deformation by earthquakes and explosions. *Bull. seism. Soc. Am.* **60**, 193–215.

Ben-Menahem, A. & Singh, S. J. 1968. Multipolar elastic fields in a layered half-space. *Bull. seism. Soc. Am.* **58**, 1519–1572.

Chinnery, M. A. 1961. The deformation of the earth around surface faults. *Bull. seism. Soc. Am.* **51**, 355–372.

Chinnery, M. A. & Jovanovich, D. B. 1972. Effects of earth layering on earthquake displacement fields. *Bull. seism. Soc. Am.* **62**, 1629–1639.

Erdelyi, A. 1954. *Tables of Integral Transforms, Vol. II.* McGraw-Hill, New York.

Iwasaki, T. & Sato, R. 1979. Strain field in a semi-infinite medium due to an inclined rectangular fault. *J. Phys. Earth* **27**, 285–314.

Jovanovich, D. B., Husseini, M. I. & Chinnery, M. A. 1974a. Elastic dislocations in a layered half-space—I. Basic theory and numerical methods. *Geophys. J. R. astr. Soc.* **39**, 205–217.

Jovanovich, D. B., Husseini, M. I. & Chinnery, M. A. 1974b. Elastic

dislocations in a layered half-space—II. The point source. *Geophys. J. R. astr. Soc.* **39**, 219–239.

Ma, X. Q. & Kusznir, N. J. 1992. 3-D subsurface displacement and strain fields for faults and fault arrays in a layered elastic half-space. *Geophys. J. Int.* **111**, 542–558.

Mansinha, L. & Smylie, D. E. 1971. The displacement fields of inclined faults. *Bull. seism. Soc. Am.* **61**, 1433–1440.

Maruyama, T. 1964. Statical elastic dislocations in an infinite and semi-infinite medium. *Bull. Earthq. Res. Inst., Tokyo Univ.* **42**, 289–368.

Mikumo, T. 1973. Faulting process of the San Fernando earthquake of February 9, 1971 inferred from static and dynamic near field displacements. *Bull. seism. Soc. Am.* **63**, 249–269.

Okada, Y. 1985. Surface deformation due to shear and tensile faults in a half-space. *Bull. seism. Soc. Am.* **75**, 1135–1154.

Okada, Y. 1992. Internal deformation due to shear and tensile faults in a half-space. *Bull. seism. Soc. Am.* **82**, 1018–1040.

Press, F. 1965. Displacements, strains, and tilts at teleseismic distances. *J. geophys. Res.* **70**, 2395–2412.

Roth, F. 1990. Subsurface deformations in a layered elastic half-space. *Geophys. J. Int.* **103**, 147–155.

Rundle, J. B. 1982. Viscoelastic-gravitational deformation by a rectangular thrust fault in a layered earth. *J. geophys. Res.* **87**, 7787–7796.

Rybicki, K. 1971. The elastic residual field of a very long strike slip fault in the presence of a discontinuity. *Bull seism. Soc. Am.* **61**, 79–92.

Sato, R. 1971. Crustal deformation due to dislocation in a multilayered medium. *J. Phys. Earth* **19**, 29–46.

Sato, R. & Matsu'ura, M. 1973. Static deformation due to the fault spreading over several layers in a multi-layered medium, Part I: Displacement. *J. Phys. Earth* **21**, 227–249.

Savage, J. C. & Hastie, L. M. 1966. Surface deformation associated with dip-slip faulting. *J. geophys. Res.* **71**, 4897–4904.

Singh, S. J. 1970. Static deformation of a multilayered half-space by internal sources. *J. geophys. Res.* **75**, 3257–3262.

Steketee, J. A. 1958a. On Volterra's dislocations in a semi-infinite elastic medium. *Can. J. Phys.* **36**, 192–205.

Steketee, J. A. 1958b. Some geophysical applications of the elasticity theory of dislocations. *Can. J. Phys.* **36**, 1168–1198.

Watterson, J. 1986. Fault dimensions, displacements and growth. *Pure & Appl. Geophys.* **124**, 355–373.

Walsh, J. J. & Watterson, J. 1987. Distributions of cumulative displacement and seismic slip on a single normal fault surface. *J. Struct. Geol.* **9**, 1039–1046.